PAPER

Crystal symmetry and polarization of high-order harmonics in ZnO

IOP Publishing Journal of Physics B: Atomic, Molecular and Optical Physics
J. Phys. B: At. Mol. Opt. Phys. **52** (2019) 225601 (12pp) https://doi.org/10.1088/1361-6455/ab470d

Crystal symmetry and polarization of high-order harmonics in ZnO

Shicheng Jiang[1,5], Shima Gholam-Mirzaei[2,5], Erin Crites[2], John E Beetar[2], Mamta Singh[2,3], Ruifeng Lu[1], Michael Chini[2,3,6] and C D Lin[4]

[1] Department of Applied Physics, Nanjing University of Science and Technology, Nanjing 210094, People's Republic of China
[2] Department of Physics, University of Central Florida, Orlando, FL 32816, United States of America
[3] CREOL, the College of Optics and Photonics, University of Central Florida, Orlando, FL 32816, United States of America
[4] J. R. Macdonald Laboratory, Department of Physics, Kansas State University, Manhattan, KS 66506, United States of America

E-mail: rflu@njust.edu.cn and Michael.Chini@ucf.edu

Received 28 July 2019, revised 30 August 2019
Accepted for publication 23 September 2019
Published 21 October 2019

Abstract

We carried out a joint theoretical and experimental study of the polarization of high-order harmonics generated from ZnO by intense, linearly-polarized, infrared laser pulses. Experimentally we found that the dependence of parallel and perpendicular polarizations on the crystal orientation for all odd harmonics are nearly identical, but they are quite different from even harmonics which also show little order dependence. A one-dimensional two-band model, combined with a linear coupled excitation model, is shown to be able to explain the observed polarization behavior, including low-order harmonics. We further note that the same odd/even order contrast have been reported in a number of other crystals, despite that the harmonics were perceived to be generated via entirely different mechanisms. We demonstrated that this universality is governed by crystal symmetry, not by specific mechanisms. Thus, polarization measurements of harmonics offers a powerful pure optical method for determining the crystal axes as well as monitoring their ultrafast changes when crystals are undergoing deformation. In addition, the ellipticity of harmonic has been studied. It shows that ellipticity of high-order harmonics from solids can be tuned precisely by changing the bond structure of the sample.

Keywords: attosecond, polarization, high-order harmonic

(Some figures may appear in colour only in the online journal)

1. Introduction

High-order harmonics generated by intense laser pulses in gases have been investigated over the last three decades as a means for providing new extreme ultraviolet and soft x-ray light sources. They are also responsible for the emergence of attosecond science [1, 2]. When harmonics are generated in the molecular frame (i.e. fixed-in-space), the anisotropy and the inherent spatial symmetry of the electronic structure of the molecule are expected to result in polarized harmonic radiation. Since gas-phase molecules can only be partially oriented, the polarization states of harmonics from molecules have been studied only rarely [3–6]. High-order harmonic generation (HHG) from solids has a much shorter history. The first experiment demonstrated HHG was from ZnO [7] using mid-infrared laser pulses. Since then, harmonics generated from various crystals have been reported [8–29], focusing largely on the dependence of harmonic yields on laser intensity and/or orientation of the crystal axis [8, 20–26]. Several experiments have also reported the polarization properties of the harmonics [22–25].

HHG from gases can be qualitatively understood using the three-step model of ionization, acceleration, and

[5] The first two authors contributed equally to this work.
[6] Author to whom any correspondence should be addressed.

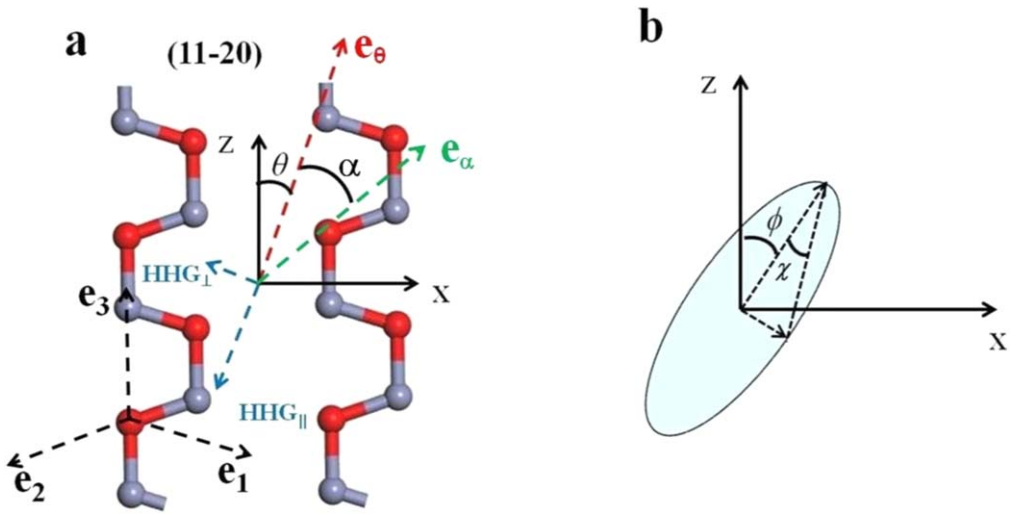

Figure 1. (a) The arrangement of atoms in real space on the (11–20) plane, red for oxygen and gray for zinc atoms. Three unit vectors $\mathbf{e_1}$, $\mathbf{e_2}$ and $\mathbf{e_3}$ are defined along the bond directions. The polarization of the driving laser makes an angle θ with respect to the crystal axis (along z). The polarization angle of the harmonic makes an angle α with respect to the polarization of the driving laser. (b) Definition of the polarization ellipse and the angle χ which is related to the ellipticity by $\epsilon = \tan(\chi)$.

recollision [30–32]. This model has been extended to the quantitative rescattering theory [33, 34], which allows the extraction of photo-recombination transition dipole matrix elements from experimental spectra. The recombination dipole is related to the photoionization transition dipole, which reflects the molecular symmetry. Such symmetry would appear in the polarization of harmonics as well; however in experiments it is blurred by molecular rotation. For harmonics from solids, the crystal axes can be precisely aligned without rotational motion, and thus experimentally-obtained harmonic polarization states are expected to reflect the crystal symmetry. Indeed, experimental harmonic spectra are observed to reveal rotational symmetry [20, 26]. However, the role of other symmetries in solids has been less studied. Here, we investigate the role of crystal symmetry properties in determining the polarization states of HHG.

For solids, time-dependent density functional theory (TDDFT) [35–37], time-dependent Schrödinger equations (TDSE) [38] and Semiconductor Bloch equations (SBEs) [39, 40] are usually used to calculate harmonics generated from solids. A three-step model similar to the case of gaseous media was also developed for two-band solid system [41]. Recently, Li *et al* proposed a four-step model to explain the anomalous ellipticity dependence of solid-HHG in momentum space [42]. The SBEs method is often favored since it offers a simple way to account for dephasing of electron trajectories. We are aware that Floss *et al* has extended the TDDFT to open quantum system taking dephasing effect into account, but such calculations are much more complicated [43]. Thus, in practical applications, one-dimensional (1D) SBEs are often employed to calculate HHG from solids. Depending on the band structure of the solid, the number of valence bands and conduction bands in the SBEs calculations can be varied. In general, multiband calculations are difficult to analyze, but this is not the case for ZnO which is dominated by two bands. Figure 1 summarizes the structure of ZnO in real space. HHG from ZnO was first studied in 2011 [7] and again in 2016 [8]. In both experiments, the dependence of harmonic spectra on crystal orientation with respect to the driving laser polarization direction were reported. Both even and odd harmonics are clearly seen in the experiments, which is consistent with the lack of inversion symmetry along the ZnO *c*-axis. However, orientation-dependent features of even harmonics in ZnO could not be reproduced theoretically until recently, when Jiang *et al* [44, 45] took the transition dipole phase into consideration. A recent review on theoretical models on solid-HHG can be found in [46]

Previous 1D calculations by Jiang *et al* [45] only obtain harmonics polarized in the same direction as the driving laser polarization. However, most measurements have not discriminated between parallel and perpendicularly polarized harmonics. While it is straightforward to extend the SBEs model to 2D or 3D, the numerical effort is large. Interestingly, a simple Linearly Coupled Excitation (LCE) model has been proposed previously by Koch and collaborators [22]. The model has been applied to calculate parallel and perpendicularly polarized harmonics in GaSe generated by THz pulses. The method involves solving the 1D SBEs for the induced current along the direction of each bond in the crystal. These bonds of course underlie the intrinsic symmetry of the crystal. The LCE model was implemented by Jiang *et al* [45] to obtain parallel and perpendicular harmonics[7] in ZnO. By including the two harmonic polarization components, improved agreement with the experimental data of [8] was observed. Still, a critical test of the model is to compare with polarization-sensitive experiments. By carrying out the LCE model calculation in conjunction with polarization-sensitive measurements, we report in this paper that the polarization states of harmonics can largely be explained by symmetry, using the LCE model.

[7] We thank Referee B of our previous paper [45] for suggesting the LCE model to obtain perpendicular harmonics.

2. Polarization properties of HHG

In the experiments, harmonics were produced in ZnO using a commercial optical parametric amplifier (Light Conversion ORPHEUS). The idler pulses, with central wavelength of 3.6 μm, energy of 10 μJ, and pulse duration of 90 fs were focused onto the exit plane of a 0.3 mm thick a-cut zinc oxide crystal. The estimated incident laser intensity is about $2 \times 10^{12}\,\mathrm{W\,cm^{-2}}$. The crystal could be rotated about its surface normal, to vary the orientation of the c-axis with respect to the laser polarization direction. The generated harmonics passed through a polarizer and were detected using a UV-enhanced spectrometer (Ocean Optics HR2000+ES) capable of detecting harmonics from 4th to 17th order. Two types of measurements were performed. In the first case, we fixed the angle between the laser polarization and the c-axis, and rotated the polarizer to analyze the polarization states of the generated harmonics. In the second set of experiments, we fixed the polarizer and varied the crystal orientation. In this case, the polarizer was set to pass harmonics generated with polarization parallel or perpendicular to the driving laser polarization, and the harmonic spectra were measured as a function of the crystal orientation. All these measurements were done using two different polarizers: a sheet polarizer (400–750 nm) was used to measure the polarization states of below-gap harmonics with photon energy below the ZnO band gap (3.3 eV), while a broadband wire grid polarizer (250–4000 nm) was used to measure the above-gap harmonics.

To understand the polarization properties of HHG, a one-dimensional two-band SBEs combined with a linear coupled excitation model is applied here. Detail of our model can be found in appendix A. In the LCE model, one calculates one-dimensional excitation components associated with three bond directions $\mathbf{e_1}$, $\mathbf{e_2}$ and $\mathbf{e_3}$, as shown in figure 1(a). The laser polarization makes an angle θ with respect to crystal's optic axis which is taken as the z-axis, and the polarization direction of harmonics are measured with respect to the laser polarization axis. Excitation along each direction is calculated using 1D two-band SBEs. It is important to use accurate band structures and dipole matrix elements with amplitudes and phases as shown in our previous work [45]. In order to obtain the polarization distribution, a new unit vector $\mathbf{e}(\alpha)$ pointing in the direction of α is defined. It can be written in terms of $\mathbf{e_1}$, $\mathbf{e_2}$ as:

$$\mathbf{e}(\alpha) = \frac{\sin(\alpha+\theta)}{2\cos(18^\circ)}(\mathbf{e_1}-\mathbf{e_2}) - \frac{\cos(\alpha+\theta)}{2\cos(72^\circ)}(\mathbf{e_1}+\mathbf{e_2}). \quad (1)$$

The current along $\mathbf{e}(\alpha)$, defined with respect to driving laser polarization, is written as

$$J(\theta,\alpha,t) = [J_1(t)\mathbf{e_1} + J_2(t)\mathbf{e_2} + J_3(t)\mathbf{e_3}]\cdot\mathbf{e}(\alpha), \quad (2)$$

where $J_j(t)$ is the current along direction $\mathbf{e_j}$. The intensity of the generated harmonics polarized along the direction with angle α can be calculated by projection:

$$I(\theta,\alpha,\omega) = |(E_1(\omega)\mathbf{e_1} + E_2(\omega)\mathbf{e_2} + E_3(\omega)\mathbf{e_3})\cdot\mathbf{e}(\alpha)|^2, \quad (3)$$

where $E_j(\omega)$ is the Fourier transform of the current along direction $\mathbf{e_j}$. In the SBEs calculation, only two bands are included.

Figure 2 shows the comparison of experimental and theoretical polarization-resolved harmonic spectra, separated into two groups: below-gap harmonics, from H4 to H10 (a)–(d), and above-gap harmonics, from H11 to H17 (e)–(h). To illustrate orientation dependence, the theory has been scaled for each harmonic to show optimal visual agreement (each harmonic has the same scaling factor for parallel and perpendicular components). In the simulation, laser intensity is set to be $9 \times 10^{10}\,\mathrm{W\,cm^{-2}}$ considering dielectric effect inside the crystal. Clearly there is a good general agreement between the experimental data and the prediction from the LCE model. While some detailed features for perpendicularly-polarized above-gap harmonics are not as clearly seen because of the low signal levels, one can see that the dominant features are similar to the below-gap harmonics.

Two particularly notable features are seen from these data. When the laser polarization is parallel to the mirror plane (e.g. $\theta = 0^\circ$ or 180°, Γ–A axis), both even and odd harmonics have strong parallel components, but the perpendicular components disappear. When the laser polarization is perpendicular to the mirror plane, (e.g. $\theta = 90^\circ$, Γ–M axis) all the parallel even harmonics and perpendicular odd harmonics vanish. It is obvious that disappearance of parallel even harmonics is attributed to the reflection symmetry. The general feature of vanishing perpendicular harmonics at specific orientation angles can also be explained by the symmetry properties of the system, as shown below. By inserting equation (1) into equation (2), the latter can be expressed as

$$\begin{aligned} J(\theta,\alpha,t) = {} & A(\theta,\alpha)(J_1(t) + \cos(144^\circ)J_2(t) \\ & + \cos(108^\circ)J_3(t)) \\ & + B(\theta,\alpha)(\cos(144^\circ)J_1(t) + J_2(t) \\ & + \cos(108^\circ)J_3(t)), \end{aligned} \quad (4)$$

where

$$A(\theta,\alpha) = \left(\frac{\sin(\alpha+\theta)}{2\cos(18^\circ)} - \frac{\cos(\alpha+\theta)}{2\cos(72^\circ)}\right),$$

$$B(\theta,\alpha) = \left(\frac{-\sin(\alpha+\theta)}{2\cos(18^\circ)} - \frac{\cos(\alpha+\theta)}{2\cos(72^\circ)}\right).$$

When α is set to 90°, we can obtain the perpendicular current. For the two special cases, e.g. $\theta = 0^\circ$ and 90°, $J(\theta = 0^\circ, \alpha = 90^\circ, t) \propto J_1(t) - J_2(t)$, and $J(\theta = 90^\circ, \alpha = 90^\circ, t) \propto J_1(t) + J_2(t)$, respectively. Using the strong field approximation (SFA)

$$\begin{aligned} J(\theta = 0^\circ, \alpha = 90^\circ, t) \propto {} & -i\omega \int_{BZ} dk \int_{-\infty}^{t} dt' D^*_{cv,e_1} \\ & \times (k + A_{e_1}(t)) F_{e_1}(t') D_{cv,e_1}(k + A_{e_1}(t')) e^{-iS(k,t,t')} \\ & + i\omega \int_{BZ} dk \int_{-\infty}^{t} dt' D^*_{cv,e_2}(k + A_{e_2}(t)) \\ & \times F_{e_2}(t') D_{cv,e_2}(k + A_{e_2}(t')) e^{-iS(k,t,t')} + \text{c.c}, \end{aligned} \quad (5)$$

where $S(k, t, t')$ is the standard action in the SFA theory and D_{cv,e_i} is the transition dipole moment. For $\theta = 0^\circ$,

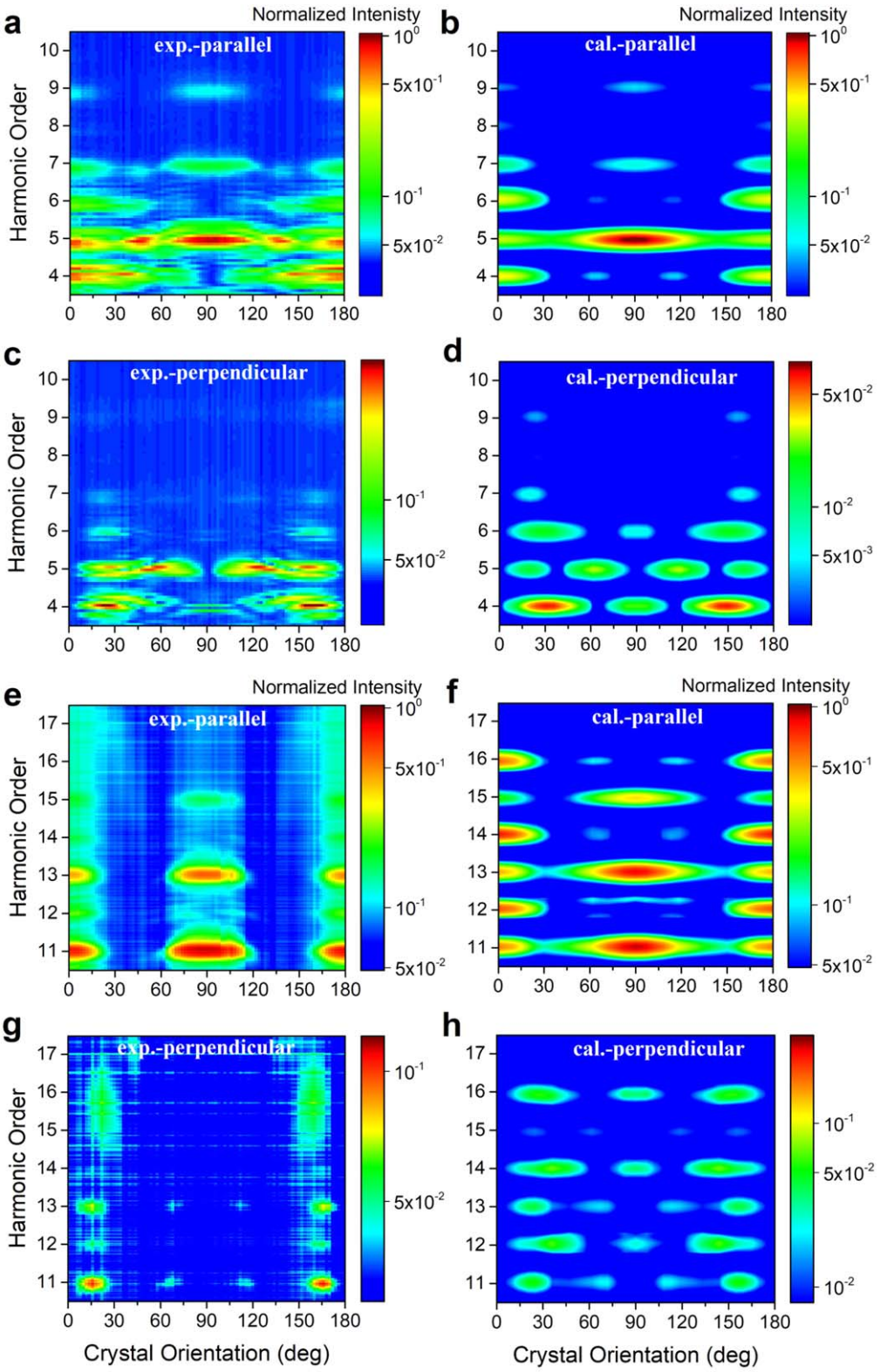

Figure 2. The left column shows the experimental results and the right column shows the simulations. The top two rows are for below-gap harmonics and the bottom two rows are for above-gap harmonics. The first row of each group is for parallel polarization component and the second row is for perpendicular polarization component. The simulation for each harmonic is normalized to experimental data separately for best visual agreement. A single scaling factor is used for both polarizations and all crystal orientations. Weaker features in above-gap harmonics in the experiment lie below the noise level.

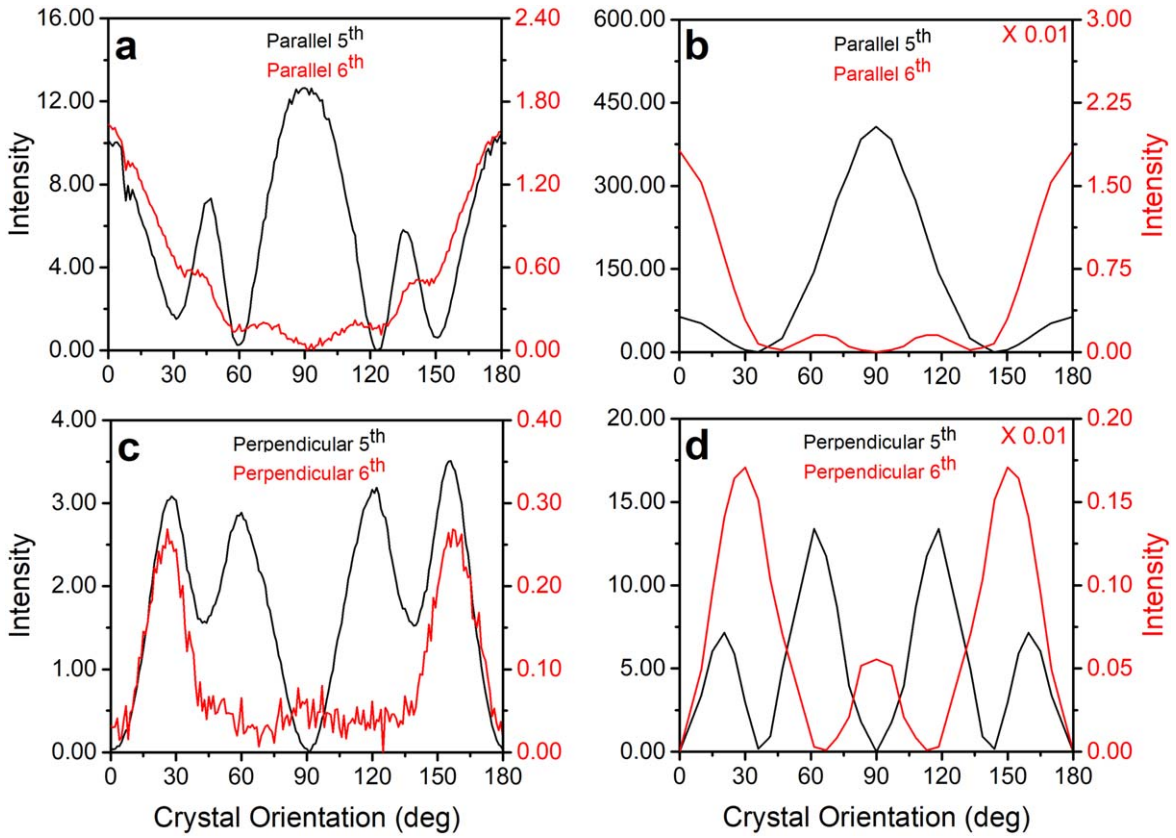

Figure 3. The top frames are for the parallel components and the bottom frames are for the perpendicular components. The left column is from experiment and the right column is from simulation. For parallel components, the additional peaks observed (a) at 45° and 135° but not seen in simulation (b) are attributed to birefringent effect, see text. For the perpendicular polarization, the positions of the maxima and minima in the experiment and simulation are identical, but the relative magnitude of the peaks differs.

$A_{e_1} = A_{e_2}, F_{e_1} = F_{e_2}, D_{cv,e_1} = D_{cv,e_2}$, which leads to $J(\theta = 0°, \alpha = 90°, t) = 0$. In turn, this leads to no perpendicular harmonic signal, for both even and odd harmonics, for $\theta = 0°$, in agreement with experimental observation and the prediction of the LCE model. Similarly, we obtain

$$\begin{aligned} J(\theta = 90°, \alpha = 90°, t) \propto & -i\omega \int_{BZ} dk \int_{-\infty}^{t} dt' D^{*}_{cv,e_1} \\ & \times (k + A_{e_1}(t)) F_{e_1}(t') D_{cv,e_1}(k + A_{e_1}(t')) \times e^{-iS(k,t,t')} \\ & - i\omega \int_{BZ} dk \int_{-\infty}^{t} dt' D^{*}_{cv,e_2}(k + A_{e_2}(t)) \\ & \times F_{e_2}(t') D_{cv,e_2}(k + A_{e_2}(t')) \times e^{-iS(k,t,t')} + \text{c.c.} \end{aligned} \quad (6)$$

For $\theta = 90°$, $A_{e_1} = -A_{e_2}$, $F_{e_1} = -F_{e_2}, D_{cv,e_1} = D_{cv,e_2}$. This means that the quantum orbit at (k_s, t'_s, t_s) and at $(k_s, t'_s + T/2, t_s + T/2)$ are always equal. This symmetry leads to the existence of pure even harmonics in the perpendicular direction, which is consistent with the prediction of the LCE model as well as the experimental observation. When the polarization of the driving laser is not parallel or perpendicular to the optic axis, both even and odd harmonics would appear in general.

To show these symmetry-imposed features more clearly, we display the polarization-resolved orientation-dependent intensities of harmonics H5 and H6 in figure 3. Similar plots for H11 and H12 are shown in the appendix B. For the parallel component of H5, the experiment shows additional peaks at about 45° and 135°. These peaks are absent in the theory. Similar weaker features also appear at H7 in the experiment, but not in above-gap harmonics. This difference is likely due to the birefringence properties [47] of bulk ZnO crystals, as discussed in appendix C. As the harmonics are generated close to the exit plane of the crystal, they are sensitive to changes in the driving laser polarization. For linearly-polarized light incident on the crystal, the polarization after propagation becomes elliptical for crystal orientation angles close to 45° and 135°. For other polarization components, all the notable features agree very well between experiment and simulation.

For a particular orientation of the crystal, we also determine the polarization states of the emitted harmonics. Specifically, we characterize the harmonic polarization for driving laser polarizations both parallel and perpendicular to the crystal *c*-axis. The results from experiment and theory for below-gap harmonics are shown in figure 4, while above-gap harmonics are shown in appendix B. We find generally good agreement between theory and simulation for each harmonic. Along the *c*-axis (upper frames), the polarization states of even and odd harmonics are quite similar since both even and odd harmonics have large parallel components, while the perpendicular components are negligible. Thus the signal decreases monotonically as the polarizer is rotated from

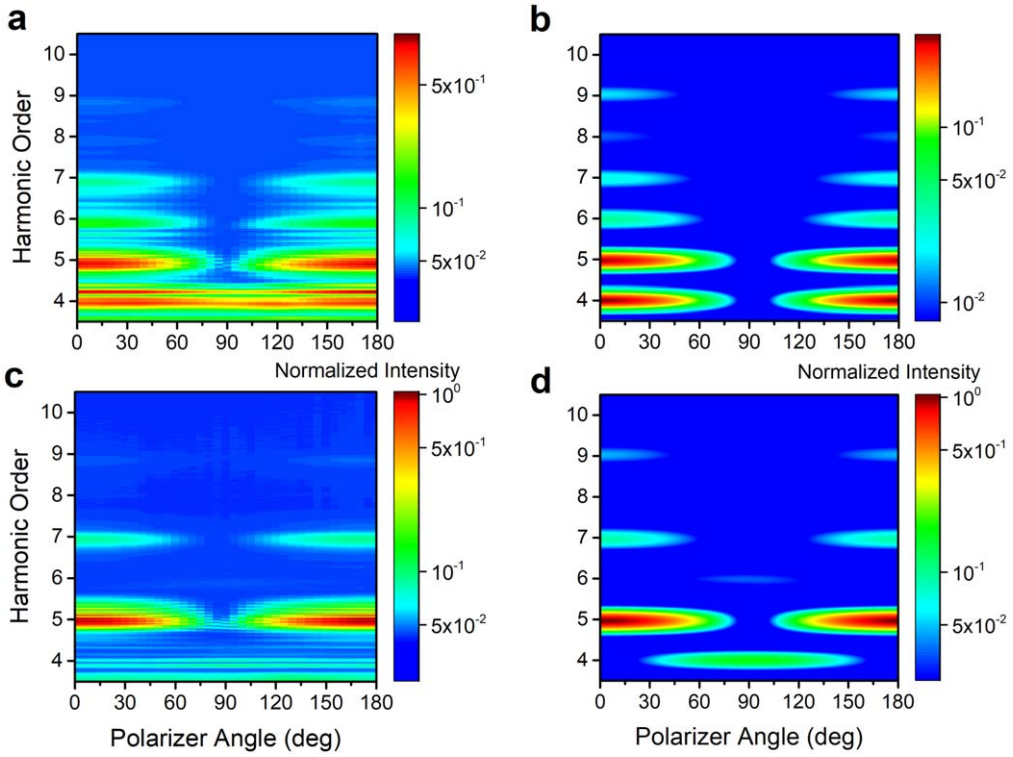

Figure 4. The driving laser is polarized parallel (top frames) or perpendicular (bottom frames) to the optic axis of the crystal. The left column is from experiment and the right column is from simulation. Each harmonic in the simulation is normalized independently for better comparison with experiment. The signals are obtained in experiment by rotating the polarizer.

$\alpha = 0°$ (180°) to 90°. When the laser polarization is perpendicular to the c-axis (lower frames), the perpendicular polarization components of odd harmonics vanish, while the parallel component is large. Thus the odd harmonics vanish at $\alpha = 90°$. On the other hand, for even harmonics, the behavior is reversed: the parallel component vanishes, while the perpendicular component is nonzero. Thus for polarizer at $\alpha = 90°$, the signal is large, and it decreases as the angle moves away from it.

3. Discussion on the mechanisms for perpendicularly polarized harmonics

The above discussion on the polarizations of harmonics concentrated only on ZnO, calculated using the 1D two-band SBEs together with the LCE model. In this case, the theory explains the experiments quite well. However, the arguments are mostly based on the symmetry of the crystal. Thus we wish to determine whether the observed behavior can be generalized to other systems. By perusing experimental polarization data for different solids, we find that most data show similarities to ZnO, provided that the symmetry properties of the material are considered. We first consider the results of [22], in which THz pulses are used to generate harmonics from GaSe. All the harmonics reported in this experiment are below the band gap. Their figures 1(c) and (d) are similar to our figure 4. Their simulation, which is based on solving the 1D SBEs with three valence bands and two conduction bands together with the LCE model, indeed also explained the observed polarization data. Polarization angle dependence was also reported in [24] for α-quartz. Their figure 2 graphs, though plotted differently, agree qualitatively with our figure 4. The perpendicular harmonics in [24] were interpreted using the intra-band Berry curvature, and thus the underlying theory appears to be different from the one used here and in [22]. Additional experimental data can be found in [23] for MoS_2 and in [25] for GaSe. All of these experimental results show general features that: (1) parallel even harmonics and perpendicular odd harmonics vanish when the laser polarization is perpendicular to the mirror plane; (2) perpendicular even and odd harmonics vanish when the laser polarization is parallel to the mirror plane.

From these results, one may conclude that many of the features of polarization-dependent HHG spectra are governed by the crystal symmetry, irrespective of the excitation 'mechanisms'. we will show that all these mechanisms, including Berry curvature, interband excitation and band curvature, are consistent with each other. Because wurtzite ZnO has broken symmetry, we have $\mathbf{D}_{m,n}(-k_x, -k_y, -k_z) = \mathbf{D}^*_{m,n}(k_x, k_y, k_z)$ for the transition dipole in a specific gauge [44, 48]. Once the system has mirror symmetry, say on the $(x = 0, y, z)$ plane, we can get $u_{m,-k_x,k_y,k_z}(x, y, z) = \pm u_{m,k_x,k_y,k_z}(-x, y, z)$ where $u_{m,\mathbf{k}}(\mathbf{r})$ is the periodic part of the Bloch eigenfunction. When '+' (−) is for band m and '−' (+) is for band n, we say they have opposite 'parities'. Otherwise, we say they have same

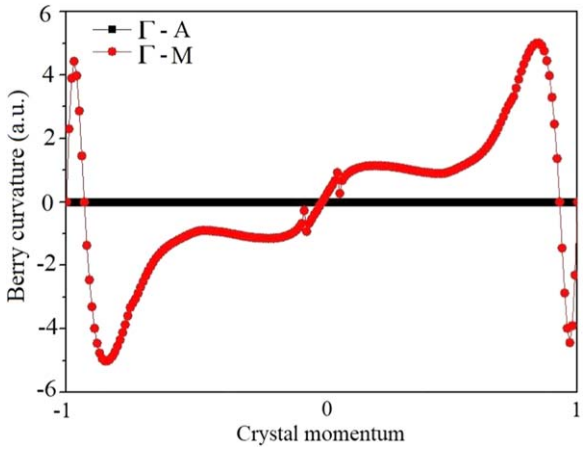

Figure 5. Berry curvature of the first conduction bands for Γ–*A* and Γ–*M*. For both of these directions, the number of *k* points is set to be 200, and 48 bands with 18 valence bands are included.

'partities'. If band *m* and band *n* have the same 'parities', we find:

$$D^x_{m,n}(-k_x, k_y, k_z) = \frac{ip^x_{m,n}(-k_x, k_y, k_z)}{\Delta E_{m,n}} = -D^x_{m,n}(k_x, k_y, k_z) \tag{7}$$

$$D^z_{m,n}(-k_x, k_y, k_z) = \frac{ip^z_{m,n}(-k_x, k_y, k_z)}{\Delta E_{m,n}} = D^z_{m,n}(k_x, k_y, k_z), \tag{8}$$

where $p^\alpha_{m,n}(\alpha = x, y, z)$ is the momentum matrix, $\Delta E_{m,n}$ is the energy difference between band *m* and band *n*. Based on these two equations, along the Γ–*A* direction where $k_x = k_y = 0$, we find that $D^x_{m,n}(k_z)$ is zero and therefore the perpendicular components of even and odd harmonics both disappear. Along the Γ–*M* direction, $k_y = k_z = 0$, and thus $D^x_{m,n}(k_x)$ and $D^z_{m,n}(k_x)$ have opposite reflection 'parities', e.g. $D^x_{m,n}(k_x)$ is an odd function and $D^z_{m,n}(k_x)$ is an even function with respect to k_x. This leads to odd and even harmonics with purely parallel and perpendicular polarizations, respectively. If the eigenfunctions of valence band and conduction band have opposite 'parities' we come to get a similar conclusion but with *z* and *x* components interchanged. These results are consistent with figure 3. The conclusion above is also consistent with the Berry curvature mechanism. From Kubo formula [49], Berry curvature is given by

$$\Omega^y_n = -\sum_{m\neq n} \frac{2Im(p^x_{n,m}p^z_{n,m})}{\Delta E^2_{m,n}}. \tag{9}$$

When the driving laser is along Γ–*A*, $p^x_{n,m}(k_z) = 0$ or $p^z_{n,m}(k_z) = 0$, $\Omega^y_n(k_z) = 0$ and no perpendicular harmonics are induced by Berry curvature. When the driving laser is along Γ–*M*, $p^x_{n,m}(k_x)$ and $p^z_{n,m}(k_x)$ are nonzero and have opposite 'parities', resulting in Berry curvature being an odd function of k_x. This would lead to purely perpendicular even harmonics according to the Berry Curvature mechanism [23]. The simulated Berry curvature Ω^y_n of the first conduction bands for Γ–*A* and Γ–*M* directions in figure 5. From the previous work [25], perpendicular harmonics can also come from band curvature. In the second-order nondegenerate perturbation theory, the band energy around $\mathbf{k_0}$ can be expressed as [50]

$$E_n(\mathbf{k}) = \mathbf{k}^2/2 + \mathbf{k}\cdot\mathbf{p}_{nn}(\mathbf{k}_0) + E_n(\mathbf{k}_0) + \sum_{\lambda\neq n}\frac{(\mathbf{k}\cdot\mathbf{p}_{n,\lambda}(\mathbf{k_0}))(\mathbf{k}\cdot\mathbf{p}_{\lambda,n}(\mathbf{k_0}))}{E_n(\mathbf{k}_0) - E_\lambda(\mathbf{k}_0)}. \tag{10}$$

Band curvature can be expressed as:

$$\frac{\partial^2 E_n(\mathbf{k})}{\partial k_i \partial k_j} = \frac{1}{m_{n,ij}} = \delta_{ij} + \sum_{\lambda\neq n}\frac{2p_{n\lambda,i}(\mathbf{k_0})p_{\lambda n,j}(\mathbf{k_0})}{E_n(\mathbf{k}_0) - E_\lambda(\mathbf{k}_0)}, \tag{11}$$

where $m_{n,ij}$ is the effective mass tensor. Thus, similar to Berry curvature in Kubo's formula, the band curvature can also be expanded by inter-band momentum matrix. Because the band curvature induced electric field $\mathbf{E}^{bc}(t) \propto \frac{F(t)}{m_{n,ij}}$, it is easy to prove that $E^{bc}_\perp(t) = E^{bc}_\perp(t + T/2)$ and $E^{bc}_{||}(t) = -E^{bc}_{||}(t + T/2)$ if the driving laser's polarization is perpendicular to miror plane. It means that all these mechanisms, including Berry curvature, interband excitation and band curvature, are consistent with each other, and polarizations of harmonics are governed by crystal symmetry, not by one of the 'mechanisms'. Thus, when such symmetry imposed constraints are not satisfied in simulations or in experiments, due care must be exercised.

4. Polarization ellipse of harmonics

From LCE model, it is clear that the polarization states of HHG are dependent on the bond structure of the crystal. Because the bonds inside crystals are fixed naturely, it is a potential way to tune the ellipse states of the HHG by changing the structures though strain or selecting crystals with specific structures. Here we show the ellipticity of HHG from wurtzite ZnO briefly. There is a phase angle in the electric fields between the two polarization components. Such phase angle can be determined experimentally in principle, but has not been done so far for harmonics from solids. If this phase angle δ is determined, then the polarization is fully described by an ellipse, see figure 1, where the ellipse is characterized by an orientation angle ϕ with respect to the polarization of the driving laser and the ellipticity ϵ. These two experimentally determined quantities ϕ and ϵ are related to parallel and perpendicular harmonics strength and the relative phase angle δ through [6]

$$\tan(2\phi) = \tan(2\gamma)\cos(\delta) \tag{12}$$

$$\sin(2\chi) = \sin(2\gamma)\sin(\delta), \tag{13}$$

where χ and γ are defined by ϵ=tan(χ) and $\tan(\gamma) = \sqrt{\frac{I_\perp}{I_{||}}}$.

Here we calculate the orientation angle and ellipticity from the LCE model for the above-gap harmonics (right column of figure 6), at crystal orientation angles $\theta = 0°$, 20°, 72° and 90°, respectively. Although the relative phase angle δ cannot be determined experimentally at present, the upper bound of ellipticity ϵ and orientation angle ϕ can be

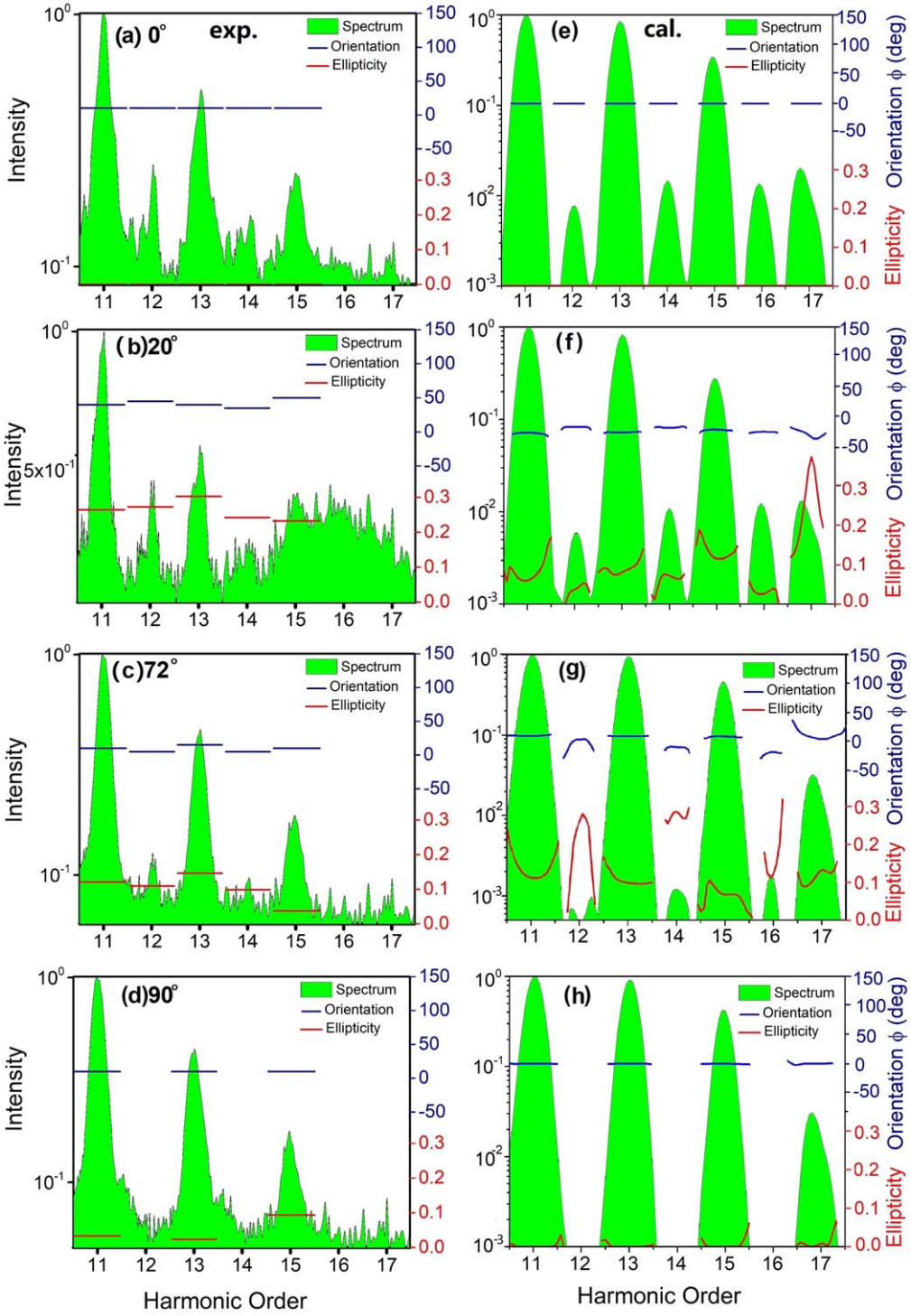

Figure 6. Left column shows experimentally extracted upper bound of ellipticity and orientation angle of the polarization ellipse of the harmonic signals. Right column shows theoretically predicted ellipticity and orientation angle of the polarization ellipse. (a), (e) $\theta = 0°$, (b), (f) $\theta = 20°$, (c), (g) $\theta = 72°$, (d), (h) $\theta = 90°$, respectively. The green area represents the harmonic spectra. Blue lines are the orientation angles and red lines are the ellipticities.

extracted by Malus' law [51] as shown in the left column of figure 6. At 0° and 90°, the harmonics are linearly polarized and the calculations are consistent with the expected results. At 20° and 72°, small ellipticity of about 0.1 and small orientation angles of about 10°–20° have been found. Their small values is consistent with the smaller perpendicular harmonic components seen in ZnO.

5. Summary

The 1D two-band SBEs model employed in our calculation is still not complete. Since the phase of the transition dipole cannot be obtained from the commercial *ab initio* codes, our calculations rely upon the tight-binding model to calculate the phase [45]. The yields for even harmonics from the present

theory appear to drop too quickly with the increase of the harmonic order, but the orientation dependence of the polarization of the harmonics agrees well with experiments. Until now, Berry curvature [23, 24], band curvature [25] and interband polarization [22] have been used to explain the perpendicular and parallel components of harmonic spectra. However, each alone is only an approximation to a complete theory that is yet to be developed. For now, a 1D SBEs model that accounts for Berry phase would be a first step toward such a theory.

In summary, we have demonstrated that polarization properties of high-order harmonics generated in ZnO can be explained using 1D two-band SBEs combined with the linearly coupled excitation (LCE) model. By comparing the existent experimental data for different systems, we emphasize that the polarization properties of high-order harmonics in solids are governed largely by the symmetry properties of the crystal. These results show that polarization of harmonics generated in a crystal provide a powerful tools for probing the spatial symmetry properties of a crystal. Using femtosecond pulses to generate harmonics, measurement of harmonic polarization states offers the opportunity to probe structural changes in a crystal with unprecedented temporal resolution.

Acknowledgments

CDL was supported in part by the Chemical Sciences, Geosciences, and Biosciences Division, Office of Basic Energy Sciences, Office of Science, U.S. Department of Energy, under Grant No. DE-FG02-86ER13491. The work done at UCF was supported by the Air Force Office of Scientific Research under Award No. FA9550-16-1-0149 and by the National Science Foundation under Grant No. 1806135. The work done at NJUST was supported by NSF of China under Grant No. 11974185 and by NSF of Jiangsu Province under Grant No. 20170032. SJ's new address is State Key Laboratory of Precision Spectroscopy, East China Normal University, Shanghai 200062, China.

Appendix A. SBEs combined with LCE model

In the model of linear combination of excitations (LCE), one calculates one-dimensional Semiconductor Bloch equations (SBEs) associated with three bond directions $\mathbf{e_1}$, $\mathbf{e_2}$ and $\mathbf{e_3}$, as shown in figure 1(a). For each direction, we use two-band SBEs model which can be written as [44]

$$\frac{\partial \rho_{cv}(\mathbf{k}, t)}{\partial t} = \left(-iE_g(\mathbf{k}) - \frac{1}{T_2}\right)\rho_{cv}(\mathbf{k}, t) + \mathbf{F}(t)\cdot\nabla_{\mathbf{k}}\rho_{cv}(\mathbf{k}, t) + i[\rho_c(\mathbf{k}, t) - \rho_v(\mathbf{k}, t)]\mathbf{F}(t)\cdot\mathbf{D}_{cv}(\mathbf{k}), \tag{A.1}$$

$$\frac{\partial \rho_v(\mathbf{k}, t)}{\partial t} = -2\,\mathrm{Im}\{\mathbf{F}(t)\cdot\mathbf{D}_{cv}(\mathbf{k})\rho_{cv}(\mathbf{k}, t)\} + \mathbf{F}(t)\cdot\nabla_{\mathbf{k}}\rho_v(\mathbf{k}, t), \tag{A.2}$$

$$\frac{\partial \rho_c(\mathbf{k}, t)}{\partial t} = 2\,\mathrm{Im}\{\mathbf{F}(t)\cdot\mathbf{D}_{cv}(\mathbf{k})\rho_{cv}(\mathbf{k}, t)\} + \mathbf{F}(t)\cdot\nabla_{\mathbf{k}}\rho_c(\mathbf{k}, t). \tag{A.3}$$

Here $\rho_{cv}(\mathbf{k}, t)$ is the micropolarization between the conduction band and the valence band. $E_g(\mathbf{k}) = E_c(\mathbf{k}) - E_v(\mathbf{k})$ is the energy difference between the two bands, $\rho_{c(v)}(\mathbf{k}, t)$ is the electron density in the conduction (valence) band. A k-dependent bell-shaped form of the dephasing time $T_2(k) = 1 + 1/[1 + \exp(100|k| - 5)$ is used in our calculation. From the SBEs, we can calculate the current $J_j(t)$ induced by the laser field along direction $\mathbf{e_j}$ by:

$$\mathbf{J}_i(t) = \sum_{\lambda=c,v}\int_{BZ}\mathbf{v}_\lambda(\mathbf{k})\rho_\lambda(\mathbf{k}, t)d\mathbf{k} + \frac{\partial}{\partial t}\int_{BZ}\mathbf{D}_{cv}(\mathbf{k})\rho_{cv}(\mathbf{k}, t)d\mathbf{k} + \text{c.c.} \tag{A.4}$$

Using the specific coordinate system and angles as defined in figure 1(a) of the main text, the current along a direction with an angle α is obtained by projection:

$$J(\theta, \alpha, t) = [J_1(t)\mathbf{e_1} + J_2(t)\mathbf{e_2} + J_3(t)\mathbf{e_3}]\cdot\mathbf{e}(\alpha). \tag{A.5}$$

Here θ is the polarization angle of the driving laser, and α is defined with respect to the laser's polarization. A detailed description of how we obtain the band structure and complex dipole moment are given in our previous paper [45]. High-order harmonics signal can be calculated by finding the Fourier-transform of the current, i.e.

$$S_{\mathrm{HHG}}(\theta, \alpha, \omega) \propto \left|\int_{-\infty}^{\infty}[\mathbf{J}(\boldsymbol{\theta}, \boldsymbol{\alpha}, \mathbf{t})(t)]e^{i\omega t}dt\right|^2. \tag{A.6}$$

Appendix B. Orientation-dependent and polarization distribution of above-gap harmonics

In figure 2 and figure 3 of the main text, it was shown that the parallel component of the below-gap harmonic H5 shows maxima at the orientation angles of 45° and 135° in the experimental data but not in the prediction of the LCE model. From figure 2(a) of the main text, such maxima also appear weakly for H7. For above-gap harmonics, the signals are weaker but these peaks are absent. In figure B1, we present the line-out of the orientation-dependent harmonics H11 and H12, for both the parallel and perpendicular components. In figure B1, clearly there are no peaks near 45° and 135°, like those seen in H5. There is a good agreement in the parallel components in H11 and H12 between the experiment and the LCE model. For the weaker perpendicular components, the agreement is also very good despite that the noise in the experiment becomes much more pronounced. Similar to figure 4 for below-gap harmonics, in figure B2 we show the polarization distributions of harmonics at two crystal orientations, for the polarization of the driving laser parallel and perpendicular to the crystal axis. The general polarization distributions for above- and below-gap harmonics are essentially identical.

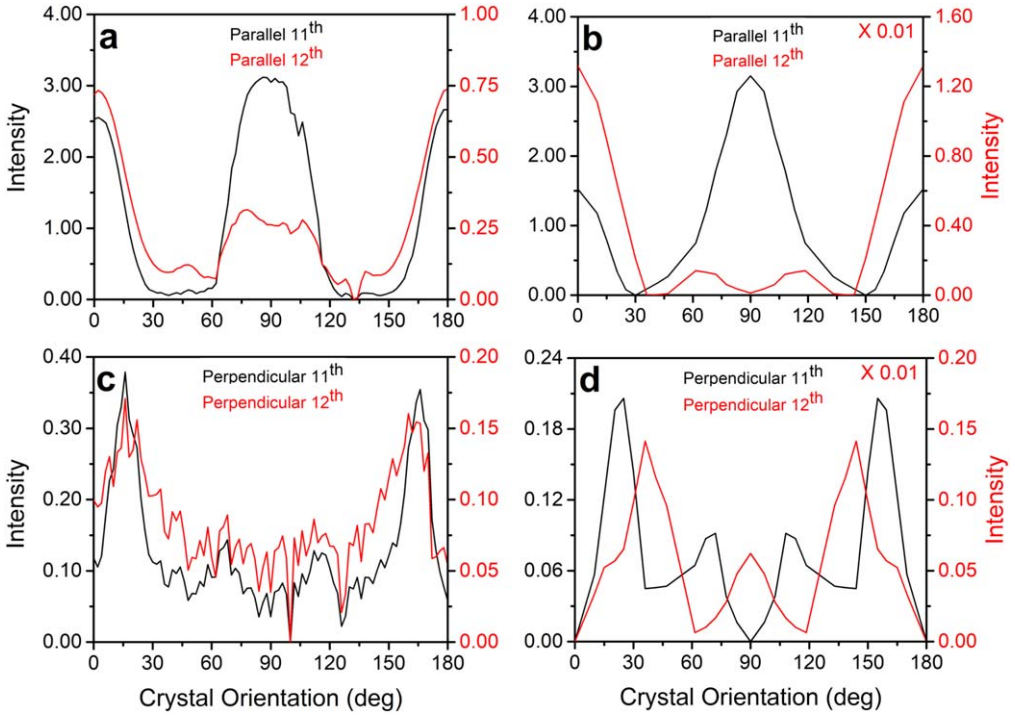

Figure B1. Orientation-dependent intensity of H11 and H12, for parallel (a), (b) and perpendicular (c), (d) components, respectively. (a), (c) are the experimental data and (b), (d) are from the simulations.

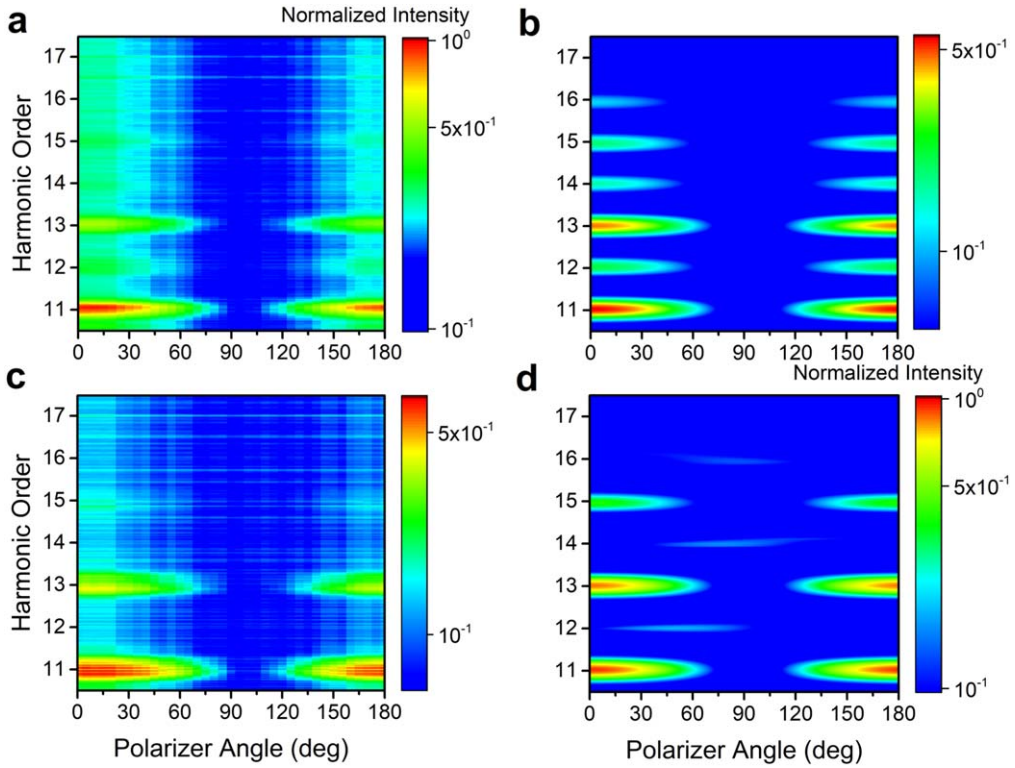

Figure B2. Polarization distribution of above-gap harmonics when the driving laser is polarized parallel [(a), (b)] and perpendicular [(c) , (d)] to the optic axis. (a), (c) are detected experimentally by rotating the polarizer, and (b), (d) are the corresponding calculated results.

Appendix C. Effects of ZnO Birefringence

The birefringence properties of ZnO may lead to undesired changes in the polarization states of both the mid-IR driving laser pulses and the generated high-order harmonics. Ideally, harmonics could be generated in a thin ZnO film; however, monocrystalline films of a-plane ZnO are not available to us at this time. Due to the experimental geometry, however,

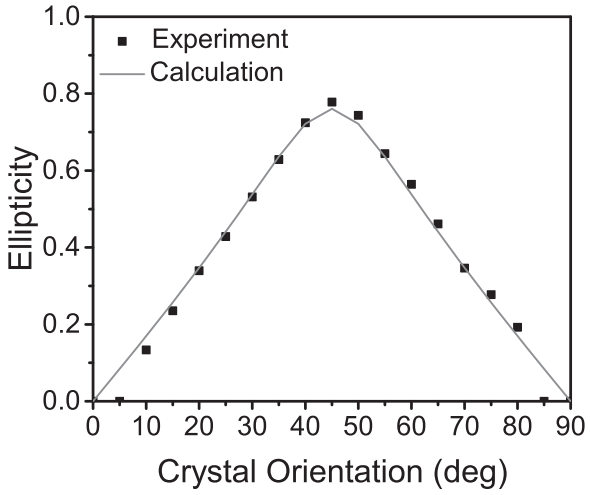

Figure C1. Orientation dependent ellipticity of driving laser at the crystal exit plane. The gray solid line shows the calculated ellipticity based on the known birefringence of ZnO and the crystal thickness of 0.3 mm.

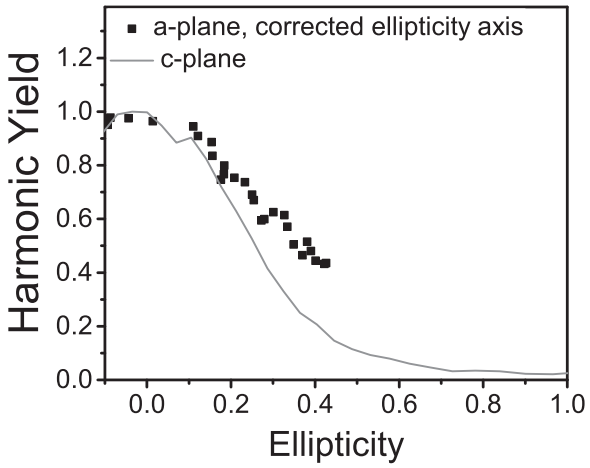

Figure C2. Dependence of 11th harmonic yield on the ellipticity of driving laser, for laser polarization in the a-plane (dots) and c-plane (solid gray line) of ZnO. For the a-plane measurements, the ellipticity of the driving laser after propagation through the crystal was measured experimentally, while for the c-plane, we confirmed that the polarization state was not changed during propagation.

harmonics are primarily generated within a small volume close to the exit plane of the crystal, and therefore the dominant role of birefringence will be to change the driving laser polarization. We have measured the ellipticity of the driving laser after propagation through the crystal under the experimental conditions. The result is shown below in figure C1. We find that the driving laser ellipticity increases from 0 to 0.8 as the orientation angle θ is increased from 0° to 45°, and then decreases back to 0 at an orientation angle of 90°. This behavior is in good agreement with the known birefringence properties of ZnO, as shown in the figure, indicating that the effects of nonlinear propagation on the polarization are small. It is well known that driving laser ellipticity affects high harmonic generation in solids [7]. However, measurements of ellipticity dependence in the a-plane of ZnO have not been reported. Figure C2 shows the ellipticity dependence of the 11th harmonic generated for laser polarization in the a-plane of ZnO. The laser ellipticity was set using a combination of a half-wave plate and a quarter-wave plate, and the data were corrected for propagation of the mid-IR laser through the birefringent crystal by measuring the mid-IR ellipticity after propagation. Due to the crystal birefringence, the maximum ellipticity obtained in this way was approximately 0.4. For comparison, we also show the measured ellipticity dependence of the 11th harmonic generated for laser polarization in the c-plane of ZnO, for which there is no birefringence. In both cases, the ellipticity dependence behaves similarly. While the harmonic generation efficiency drops substantially at relatively large values of ellipticity, it remains above 50% for ellipticity values $\leqslant 0.35$, corresponding to crystal orientation angles between 0°–20°, 70°–110°, and 160°–180°. Therefore, we can attribute the discrepancies between theory and experiments close to 45° and 135° as resulting from the elliptically-polarized driving laser.

ORCID iDs

Shima Gholam-Mirzaei https://orcid.org/0000-0002-3209-7666
Ruifeng Lu https://orcid.org/0000-0002-1752-2070
Michael Chini https://orcid.org/0000-0002-9058-928X

References

[1] Drescher M *et al* 2001 *Science* **291** 1923–7
[2] Paul P M *et al* 2001 *Science* **292** 1689–92
[3] Levesque J *et al* 2007 *Phys. Rev. Lett.* **99** 243001
[4] Zhou X *et al* 2009 *Phys. Rev. Lett.* **102** 073902
[5] Mairesse Y *et al* 2008 *New J. Phys.* **10** 025028
[6] Le A-T *et al* 2010 *Phys. Rev.* A **85** 023814
[7] Ghimire S *et al* 2011 *Nat. Phys.* **7** 138
[8] Gholam-Mirzaei S *et al* 2017 *Appl. Phys. Lett.* **110** 061101
[9] Vampa G *et al* 2015 *Nature* **522** 462
[10] Vampa G *et al* 2015 *Phys. Rev. Lett.* **115** 193603
[11] Wang Z *et al* 2017 *Nat. Commun.* **8** 1686
[12] Ghimire S 2014 *J. Phys. B: At. Mol. Opt. Phys.* **47** 204030
[13] You Y S *et al* 2017 *Opt. Lett.* **42** 1816
[14] Luu T T *et al* 2015 *Nature* **521** 498
[15] Garg M *et al* 2016 *Nature* **538** 359
[16] You Y S *et al* 2017 *Nat. Commun.* **8** 724
[17] Hohenleutner M *et al* 2015 *Nature* **523** 572
[18] Yoshikawa N *et al* 2017 *Science* **356** 736
[19] Taucer M *et al* 2017 *Phys. Rev.* B **96** 195420
[20] You Y S *et al* 2017 *Nat. Phys.* **13** 345
[21] Schubert O *et al* 2014 *Nat. Photon.* **8** 119
[22] Langer F *et al* 2017 *Nat. Photon.* **11** 227
[23] Liu H *et al* 2016 *Nat. Phys.* **13** 262
[24] Luu T T and Wörner H J 2018 *Nat. Commun.* **9** 916
[25] Kaneshima K *et al* 2018 *Phys. Rev. Lett.* **120** 243903
[26] You Y S *et al* 2018 *J. Phys. B: At. Mol. Opt. Phys.* **51** 114002
[27] Gholam-Mirzaei S *et al* 2018 *J. Opt. Soc. Am.* B **35** A27–31
[28] Ndabashimiye G *et al* 2016 *Nature* **534** 520
[29] Lanin A A 2017 *Optica* **4** 516
[30] Krause J L *et al* 1992 *Phys. Rev. Lett.* **68** 3535
[31] Corkum P B 1993 *Phys. Rev. Lett.* **71** 1995
[32] Lewenstein M *et al* 1994 *Phys. Rev.* A **49** 2117

[33] Lin C D *et al* 2018 *Attosecond and Strong-Field Physics: Principles and Applications* (Cambridge: Cambridge University Press)
[34] Le A-T *et al* 2009 *Phys. Rev.* A **80** 013401
[35] Runge E and Gross E K U 1984 *Phys.Rev. Lett.* **52** 997
[36] Tancogne-Dejean N *et al* 2017 *Phys. Rev. Lett.* **118** 087403
[37] Floss I *et al* 2018 *Phys. Rev.* A **97** 011401
[38] Wu M X *et al* 2015 *Phys. Rev.* A **91** 043839
[39] Golde D *et al* 2008 *Phys. Rev.* B **77** 075330
[40] Luu T T and Wörner H J 2016 *Phys. Rev.* B **94** 115164
[41] Vampa G *et al* 2015 *Phys. Rev.* B **91** 064302
[42] Li L *et al* 2019 *Phys. Rev. Lett.* **122** 193901
[43] Floss I *et al* 2019 *Phys. Rev.* B **99** 224301
[44] Jiang S C *et al* 2017 *Phys. Rev.* A **96** 053850
[45] Jiang S C *et al* 2018 *Phys. Rev. Lett.* **120** 253201
[46] Yu C, Jiang S C and Lu R F 2019 *Adv. Phys.* X **4** 1562982
[47] Xia P *et al* 2018 *Opt. Express* **26** 29393
[48] Blount E I 1962 *Formalisms of Band Theory In Solid State Physics* vol 13 (New York: Academic) pp 305–73
[49] Yao Y *et al* 2004 *Phys. Rev. Lett.* **92** 037204
[50] Haug H and Koch S W 2009 *Quantum Theory of the Optical and Electronic Properties of Semiconductors* 5th edn (Singapore: World Scientific)
[51] Hecht E 2001 *Optics* 4th edn (Reading, MA: Addison-Wesley)